

Milli-Tesla quantization enabled by tuneable Coulomb screening in large-angle twisted graphene

Received: 16 January 2025

Accepted: 22 July 2025

Published online: 11 August 2025



I. Babich^{1,2}✉, I. Reznikov^{1,2}, I. Begichev^{1,2}, A. E. Kazantsev³, S. Slizovskiy^{3,4}, D. Baranov², M. Šiškins², Z. Zhan⁵, P. A. Pantaleon⁵, M. Trushin^{1,2}, J. Zhao², S. Grebenchuk², K. S. Novoselov^{1,2}, K. Watanabe⁶, T. Taniguchi⁷, V. I. Fal'ko^{3,4}, A. Principi³ & A. I. Berdyugin^{1,8}✉

The electronic quality of graphene has improved significantly over the past two decades, revealing novel phenomena. However, even state-of-the-art devices exhibit substantial spatial charge fluctuations originating from charged defects inside the encapsulating crystals, limiting their performance. Here, we overcome this issue by assembling devices in which graphene is encapsulated by other graphene layers while remaining electronically decoupled from them via a large twist angle ($\sim 10\text{--}30^\circ$). Doping of the encapsulating graphene layer introduces strong Coulomb screening, maximized by the sub-nanometer distance between the layers, and reduces the inhomogeneity in the adjacent layer to just a few carriers per square micrometre. The enhanced quality manifests in Landau quantization emerging at magnetic fields as low as ~ 5 milli-Tesla and enables resolution of a small energy gap at the Dirac point. Our encapsulation approach can be extended to other two-dimensional systems, enabling further exploration of the electronic properties of ultrapure devices.

Electron mobility is a critical figure of merit for semiconductors, relevant for observation of quantum phenomena and electronic applications^{1–8}. Recently, graphene was established as a material with the highest room-temperature mobility^{9,10} $\sim 150,000\text{ cm}^2\text{V}^{-1}\text{s}^{-1}$ which is two orders of magnitude higher than that of traditional semiconductors. However, the graphene mobility at cryogenic temperatures is still lower than that of GaAs two-dimensional electron gases (2DEGs), which electronic quality has been gradually improving over many decades^{4–7}, and these days can reach⁸ $57 \times 10^6\text{ cm}^2\text{V}^{-1}\text{s}^{-1}$ under optimal doping. In contrast, state-of-the-art graphene devices reach mobilities^{9–24} of only $(1\text{--}3) \times 10^6\text{ cm}^2\text{V}^{-1}\text{s}^{-1}$, an order of magnitude lower. Potentially, this discrepancy should vanish close to the charge

neutrality point (CNP), where graphene mobility theoretically diverges. However, in real devices, the electron transport near the CNP is strongly affected by the macroscopic spatial charge fluctuations^{10,21–28}, usually referred to as electron-hole puddles²⁸, limiting graphene performance.

In the first generation of devices, graphene was placed on top of Si/SiO₂ substrate^{1–3}, where it was influenced by contamination from the environment, surface roughness, and impurities, which limited mobility to $\mu \approx 10^4\text{ cm}^2\text{V}^{-1}\text{s}^{-1}$ and caused substantial charge density fluctuations of $\delta n \sim 10^{11}\text{--}10^{12}\text{ cm}^{-2}$. A significant improvement was achieved through the encapsulation of graphene with atomically flat hexagonal boron nitride (hBN) dielectric crystals^{9–24}, which reduced charge

¹Department of Materials Science and Engineering, National University of Singapore, Singapore, Singapore. ²Institute for Functional Intelligent Materials, National University of Singapore, Singapore, Singapore. ³Department of Physics and Astronomy, University of Manchester, Manchester, UK. ⁴National Graphene Institute, University of Manchester, Manchester, UK. ⁵Imdea Nanoscience, Madrid, Spain. ⁶Research Centre for Electronic and Optical Materials, National Institute for Material Science, Tsukuba, Japan. ⁷Research Centre for Materials Nanoarchitectonics, National Institute for Material Science, Tsukuba, Japan. ⁸Department of Physics, National University of Singapore, Singapore, Singapore. ✉e-mail: ian.babich@u.nus.edu; alexey@nus.edu.sg

inhomogeneity to $\delta n \sim 10^{10} \text{ cm}^{-2}$, and improved mobility to $\sim 10^6 \text{ cm}^2 \text{ V}^{-1} \text{ s}^{-1}$. Further progress was made by using graphite gates^{16–20} instead of silicon, suppressing inhomogeneity to $\delta n \sim 5 \times 10^9 \text{ cm}^{-2}$, and establishing the current benchmark for state-of-the-art devices. Such devices enabled electron transport studies at the CNP near the room temperature, revealing properties of Dirac plasma^{10,21–24}. However, at cryogenic temperatures, electron-hole puddles continue to dominate the electronic properties of graphene near the CNP. The better performance to date has been achieved in suspended graphene devices, where the dielectric substrate is eliminated, allowing charge inhomogeneity as low as^{3,29–31} $\delta n \sim 4 \times 10^8 \text{ cm}^{-2}$ and enabling to approach the Dirac point within 1 meV. However, such devices are impractical for most applications because of the challenges in fabricating dual-gated or multilayer freestanding structures.

The difference in quality between suspended and hBN-encapsulated devices is typically attributed to charged defects inside encapsulating hBN crystals, which results in charge inhomogeneity in graphene. While room for further improvement of hBN crystal quality is limited, this issue could potentially be addressed by employing Coulomb screening. Namely, a layer with a high density of states (DoS) in close proximity to graphene should suppress the electric field from charged defects and associated charge inhomogeneity.

Previous studies on Coulomb screening have utilized graphite or graphene as screening layers separated from the studied graphene by 3–10 nm thick hBN spacers^{14,24,32}. While those efforts have enabled the observation of screening-induced Anderson localization³² and suppressed particle-particle collisions^{14,24,33}, they did not result in a notable improvement of the device quality. As the screening depends exponentially on the distance¹⁴, it is essential to position the screening layer much closer to the graphene than the charged defects (see Supplementary Note 6). This makes commonly used hBN spacers impractical for electron-hole puddle screening, as charged defects, which are also present inside these crystals, are located closer to graphene than the screening layer.

In this work, we address this challenge by stacking graphene layers directly atop one another and intentionally decoupling them using a large twist angle $\theta \sim 10 - 30^\circ$. The suppressed interlayer tunneling and decoupled spectra of graphene layers in such heterostructures^{34–40} result in significant interlayer resistance^{34,38}. This allowed us to selectively charge one of the graphene layers in such devices and use it as a charged screening substrate separated from the test layer by a sub-nanometer vdW gap.

Results

Figure 1a shows one of our large-angle twisted bilayer graphene (LATBG) devices with a twist angle of $\theta \sim 20^\circ$ (See “Methods” for the details of the device fabrication). Using gold top and graphite bottom gates we can independently set the out-of-plane displacement field D and the total charge density n_{tot} .

Firstly, we characterized the LATBG device by measuring its resistance at zero D , as shown in Fig. 1b. Under such conditions, both layers have the same doping, and the system behaves similarly to single-layer graphene: resistance sharply peaks at zero carrier density and rapidly drops when doping increases. Using this curve, we estimate inhomogeneity of individual layers $\delta n \sim 7 \times 10^9 \text{ cm}^{-2}$, and electron mobility $\mu_e = 0.5 \times 10^6 \text{ cm}^2/\text{Vs}$ (Supplementary Fig. 1), which is consistent with that of a typical high-quality encapsulated devices reported in the literature^{9–24}.

Qualitatively, the applied D creates an interlayer potential difference that separates the Dirac cones in energy, whereas n_{tot} moves the common Fermi level (see inset Fig. 1b). When the Fermi level crosses the Dirac points, it is reflected as resistivity wiggles at positive and negative doping levels, as shown in Fig. 1b. The dual-gate map in Fig. 1c further shows how Dirac cone offset evolves upon changing D . Dashed lines mark the expected positions of Dirac points of top and bottom

layers which coincide well with resistivity features that we attributed to CNPs earlier.

Screening enabled quantization in milli-Tesla magnetic field

Next, to test the device quality, we measured Landau fan diagrams under different displacement fields. When $D = 0 \text{ V/nm}$ (Fig. 1d) LATBG shows a typical Landau fan diagram of single-layer graphene, but with doubled filling factors, as expected for two graphene layers with equal doping. The applied D significantly alters this picture: in Fig. 1e, there are two sets of fan diagrams converging around $n_{\text{tot}} = \pm 0.4 \times 10^{12} \text{ cm}^{-2}$, which correspond to the expected positions of the top and bottom graphene CNPs. These fans can be attributed to the individual quantization of the top and bottom layers, and their parabolic-like shape originates from the presence of the other heavily doped layer (see the schematic band structure in Fig. 2a and Supplementary Note 1). If plotted as a function of the charge density in top or bottom layer, the fan diagrams restore their linearity (Supplementary Fig. 2) and become similar to those shown in Fig. 1d.

An important difference between the fan diagrams observed in Fig. 1d, e is the magnetic field required to resolve the onset of Landau quantization. At $D = 0 \text{ V/nm}$, Landau levels (LLs) become resolvable around $B^* \approx 100 \text{ mT}$, while the applied displacement field significantly lowers this onset. To determine the onset of oscillations under an applied D we have zoomed into a small magnetic field range, as shown in Fig. 2b. In this map, the signatures of Landau fans become visible already at $B^* = 5 - 6 \text{ mT}$ (see Supplementary Fig. 11 and Supplementary Note 5), which is an order of magnitude better than the magnetic field required to see the Landau quantisation at zero D in LATBG and in test graphene devices without proximity screening (Supplementary Fig. 8).

A reduction of magnetic field required to resolve the onset of quantization in Figs. 1e and 2b indicates a decrease of charge inhomogeneity δn under applied D . Qualitatively, to resolve the first cyclotron gap in graphene, the fluctuations of the Fermi level must be smaller than the size of the first cyclotron gap³⁰. To crosscheck this criterion, we modelled DoS of graphene for given inhomogeneity level, magnetic field and temperature as a function of Fermi level and energy fluctuations δE (see Supplementary Fig. 9 and Supplementary Note 4). When $D = 0 \text{ V/nm}$ and $B^* = 100 \text{ mT}$ (B^* is the smallest magnetic field allowing resolution of the first LL), the model suggests $\delta n \approx 5 \times 10^9 \text{ cm}^{-2}$, which agrees with earlier estimations. Under applied D (for $B^* = 5 - 6 \text{ mT}$) we find that inhomogeneity drops to $\delta n \approx 2 - 3 \times 10^8 \text{ cm}^{-2}$, corresponding to just 2–3 electrons per micrometre area of the Hall bar shown in Fig. 1a. However, at small magnetic fields, the cyclotron radius R_c becomes comparable to the width of our voltage probes W , which possibly limits the resolution of quantization onset. To show this, in Fig. 2c, we plotted the $W = 2R_c$ condition, which well describes the onset of Landau quantization in our device, indicating that the quality of the LATBG device likely to be even better than estimated above. Finally, while quantization becomes apparent already at 5–6 mT, we estimate that the quantum Hall effect fully onsets at 13 mT (see Supplementary Note 5). However, at low B , zero resistivity within the cyclotron gaps is not observed because of parallel conduction through the second strongly doped layer, which remains non-quantized and contributes a significant background signal.

The suppression of δn under applied displacement field originates from the tuneable screening, in agreement with the design of our experiment. The screening of an external electric field by metallic layers is set by the DoS around the Fermi energy, which drops to zero when both layers are simultaneously tuned towards CNP ($D = 0$ case). As a result, any charged impurities within the encapsulating hBN crystals create substantial spatial fluctuations in carrier density, as illustrated in the top panel of Fig. 2c. On the contrary, the applied D

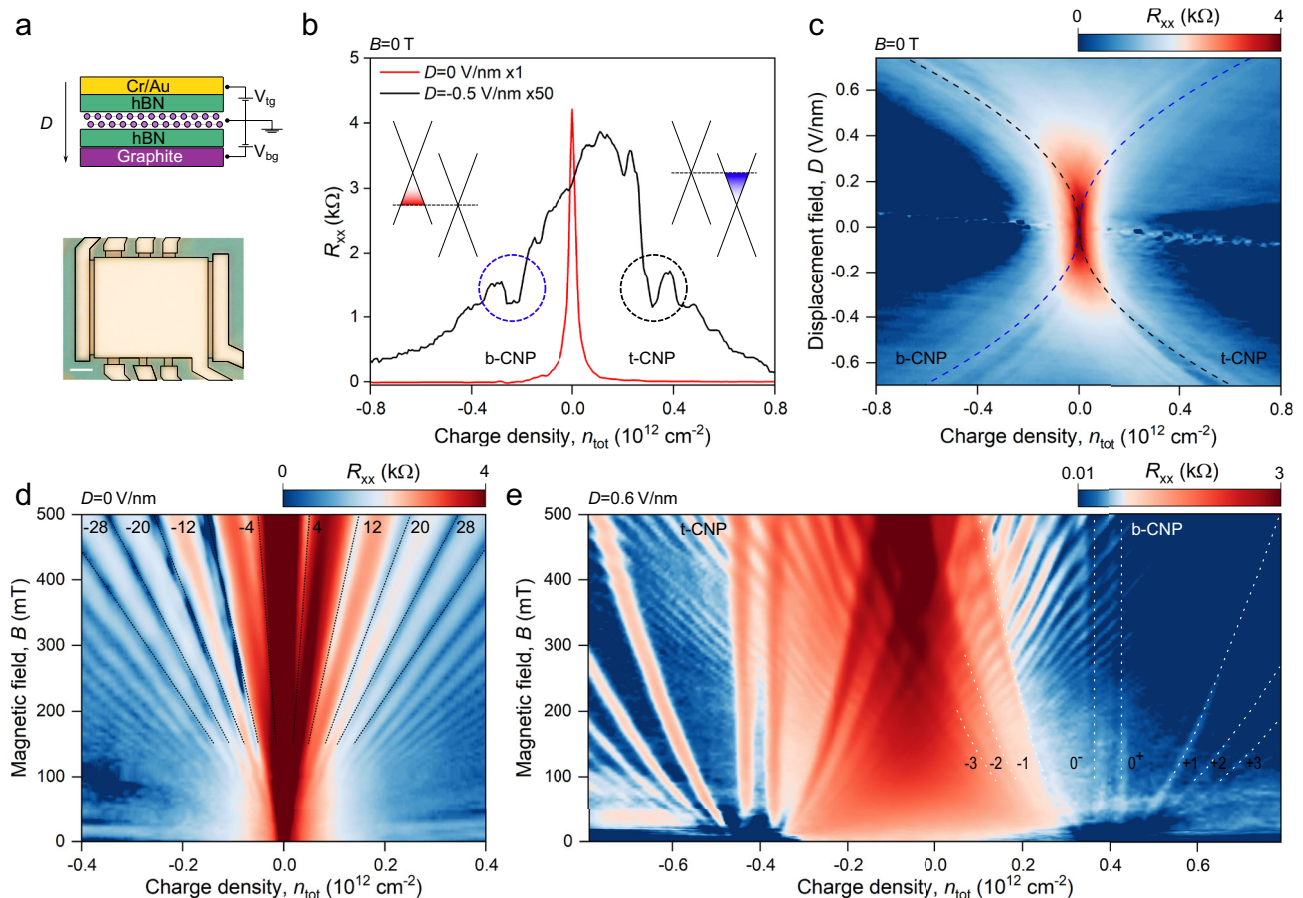


Fig. 1 | Characterization of a large-angle twisted bilayer graphene (LATBG) device. **a** Top panel: schematic structure of LATBG device, utilizing thin hBN flakes as dielectrics for bottom graphene and top metal gates, V_{tg} and V_{bg} are top and bottom gate voltages; bottom panel: optical image of LATBG Hall bar device. Black line highlights the metallic top gate and electrical contacts. Scale bar is 1 μm . **b** Longitudinal resistivity as a function of total charge density n_{tot} for $D = 0 \text{ V/nm}$, and $D = 0.5 \text{ V/nm}$ measured at zero magnetic field. Dashed circles indicate the positions of charge neutrality points of top (t-CNP, black circle) and bottom graphene layers (b-CNP, blue circle) calculated using the electrostatic model (see Supplementary Note 1). Insets schematically show band structure of LATBG under applied D when the Fermi level crosses the CNP of one of the graphene layers; here, the red part of the cone represents hole doping, and blue represents electron

doping of graphene. **c** Longitudinal resistivity at $B = 0 \text{ T}$ as a function of n_{tot} and D . Dashed lines indicate expected positions of CNPs. **d**, **e** Resistivity as a function of magnetic field B and n_{tot} for $D = 0 \text{ V/nm}$ (**d**) and $D = 0.6 \text{ V/nm}$ (**e**). In (**d**) dashed lines show the expected position of doubled graphene filling factors. In (**e**) white dashed lines are a guide for the eye of the first three Landau levels and CNP gap boundaries in bottom graphene layer. See the text for the further discussion. Further examples of Landau fan measurements are shown in Supplementary Figs. 2 and 4. The high magnetoresistance observed around $n_{\text{tot}} = 0$ can be attributed to the compensated semimetal state, similar to ref. 24, which naturally forms under applied D when one layer is electron-doped and the other is hole-doped. Measurements were performed at 2 K for all panels.

creates an energy offset between Dirac cones of different layers which entails that the double layer device has high DoS even when one of graphene layers is tuned towards the CNP. It results in screening of external electric field and improves the homogeneity of graphene layers, as shown in bottom panel of Fig. 2c. This behavior can be quantitatively described using the Thomas–Fermi model (see Supplementary Note 6) and 2D maps in Fig. 2d, which show how the screening layer suppresses charge inhomogeneity. We also note that the analysis above primarily focuses on the energy gap between the 0th and 1st Landau levels. This gap is the largest and, due to the low intrinsic doping of graphene at this filling, is expected to be the most sensitive to external screening. In contrast, higher Landau level gaps typically emerge only at larger carrier densities, where enhanced self-screening within the quantized graphene layer reduces its susceptibility to external screening.

Resolving the gap at the CNP of graphene layers

Another notable difference between the measurements at zero and the applied D is the presence of two magnetic field-independent resistance peaks in the centres of the fan diagrams of each graphene layer in

Figs. 1e and 2b. To understand these features, we perform spectroscopy of the top layer by plotting its fan diagram as a function of chemical potential in the bottom layer μ_b , see Fig. 2b. The theoretical positions of the first few LLs, indicated by dashed lines, align well with the resistivity features on this map, except that instead of a single vertical resistivity peak expected for zero-energy LL, there are two peaks. This suggests the formation of a gap at the CNPs, estimated to be $\Delta_g = 5 \pm 1 \text{ meV}$ in both layers. Furthermore, we found that the gap is present even at zero magnetic field, as shown in high-resolution fan diagram, magnetic focusing measurements, and bulk-current fan diagram (Supplementary Figs. 2 and 4). It is independent of D and becomes resolvable already at $D = 0.05 \text{ V/nm}$ (see Supplementary Figs. 3 and 5).

To verify the presence of the band gap, we modelled the fan diagram of a double layer graphene system, assuming a gap at the CNP of the quantized layer. Usually, such a gap should produce a local resistance maximum, which is not observed in our devices. To reproduce the measurements shown in Fig. 2b, we had to additionally assume valley decoupling in the gapped graphene layer, as discussed in Supplementary Note 7, which leads to the edge conductivity

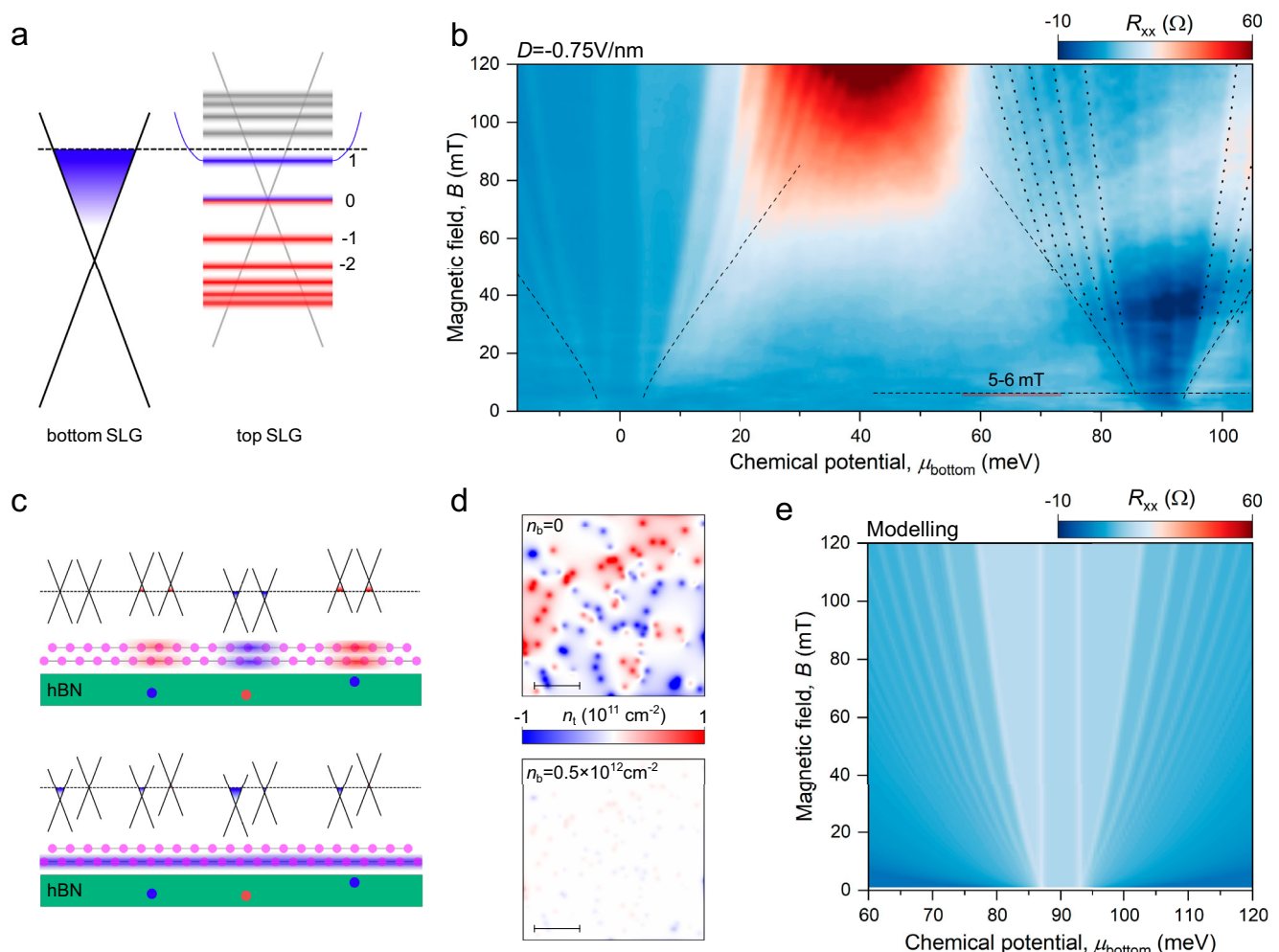


Fig. 2 | Resolving the onset of Landau quantization in milli-Tesla magnetic field.

a Schematic illustration of LATBG band structure at low magnetic field B and high D when Fermi level is tuned close to the CNP of one of graphene layers. **b** Fan diagram measured at $D = -0.75 \text{ V/nm}$ and 2 K shown as a function of chemical potential in the bottom graphene layer μ_b . Black parabolic dashed lines indicate the expected position for the first five Landau levels (LLs) plotted using a standard graphene sequence $E_N = \sqrt{2\hbar e v_F^2 N + \Delta^2}$, where \hbar is the reduced Planck constant, e is the electron charge, E_N is the energy of the N^{th} LL, and v_F is the Fermi velocity in graphene, 2Δ is a band gap discussed further in the text. The horizontal dashed line and the error bar mark the onset of Landau quantisation. Square root dashed lines

indicate the limit of quantization set by the probe width (see Supplementary Note 5). **c** Schematic illustrations of electron-hole puddles in LATBG at zero (top) and under applied (bottom) displacement fields. Red and blue shaded regions represent positive and negative doping correspondingly, coloured circles in the hBN illustrate charged defects. **d** Simulated charge density profiles in top graphene calculated for hBN with impurity density $n_{\text{imp}} = 10^{10} \text{ cm}^{-2}$ at zero doping of the bottom layer $n_b = 0$, and for $n_b = 0.5 \times 10^{12} \text{ cm}^{-2}$ (see Supplementary Note 6). Scale bars are 250 nm. **e** Modelling of LATBG resistance subjected to high D under the assumption of a gapped graphene spectra (see Supplementary Note 7).

channels inside the gap. The results of our modelling, Fig. 2e, capture the measurements shown in Fig. 2b, confirming that the two vertical resistance peaks originate from the gap edges, with their separation set by the gap size. The possible origin of this gap is discussed further in the text.

Graphene fully encapsulated with screening graphene layers

Apart from LATBG devices, where graphene serves as a substrate for another graphene layer, we fabricated large-angle twisted trilayer graphene (LATTG) devices to showcase full encapsulation of the middle graphene layer. Optical images of fabricated devices are shown in Fig. 3a. See “Methods” for fabrication details.

To characterize LATTG, we firstly measured resistance as a function of D and n_{tot} , as shown in Fig. 3b. Similar to bilayer devices, the resistance map reveals features that evolve under an applied displacement field. Using an extended electrostatic model (see Supplementary Note 1), we identified these features as the CNPs of the individual graphene layers, indicated by dashed lines in Fig. 3b. While

symmetry considerations suggest that the middle-layer CNP (m-CNP) should remain independent of D , the m-CNP in Fig. 3b shifts towards negative doping with increasing D . This behavior is reproducible across all our devices and can be explained by small energy offsets of outer graphene layers interfacing hBN³⁹.

Next, we measured the same D vs. n_{tot} map at a small magnetic field of $B = 50 \text{ mT}$, as shown in Fig. 3c. At this field, all three layers become quantized and produce three sets of parallel resistivity lines (labeled by corresponding LL number). There are single resistivity peaks corresponding to zeroth LLs in top and middle layer, while in the bottom layer, the peak doubles (labeled as 0^+ and 0^-). This feature, similarly to observations in LATBG, corresponds to the formation of a gap. However, in this LATTG device, the gap is resolved only in one of the layers.

To further assess the quality of our LATTG devices, we measured fan diagrams under fixed D or n_{tot} , shown in Fig. 3d–g and Supplementary Fig. 22. In all LATTG devices, we observed three sets of Landau fans converging at carrier densities corresponding to the expected positions of the CNPs for individual layers, as indicated by the arrows

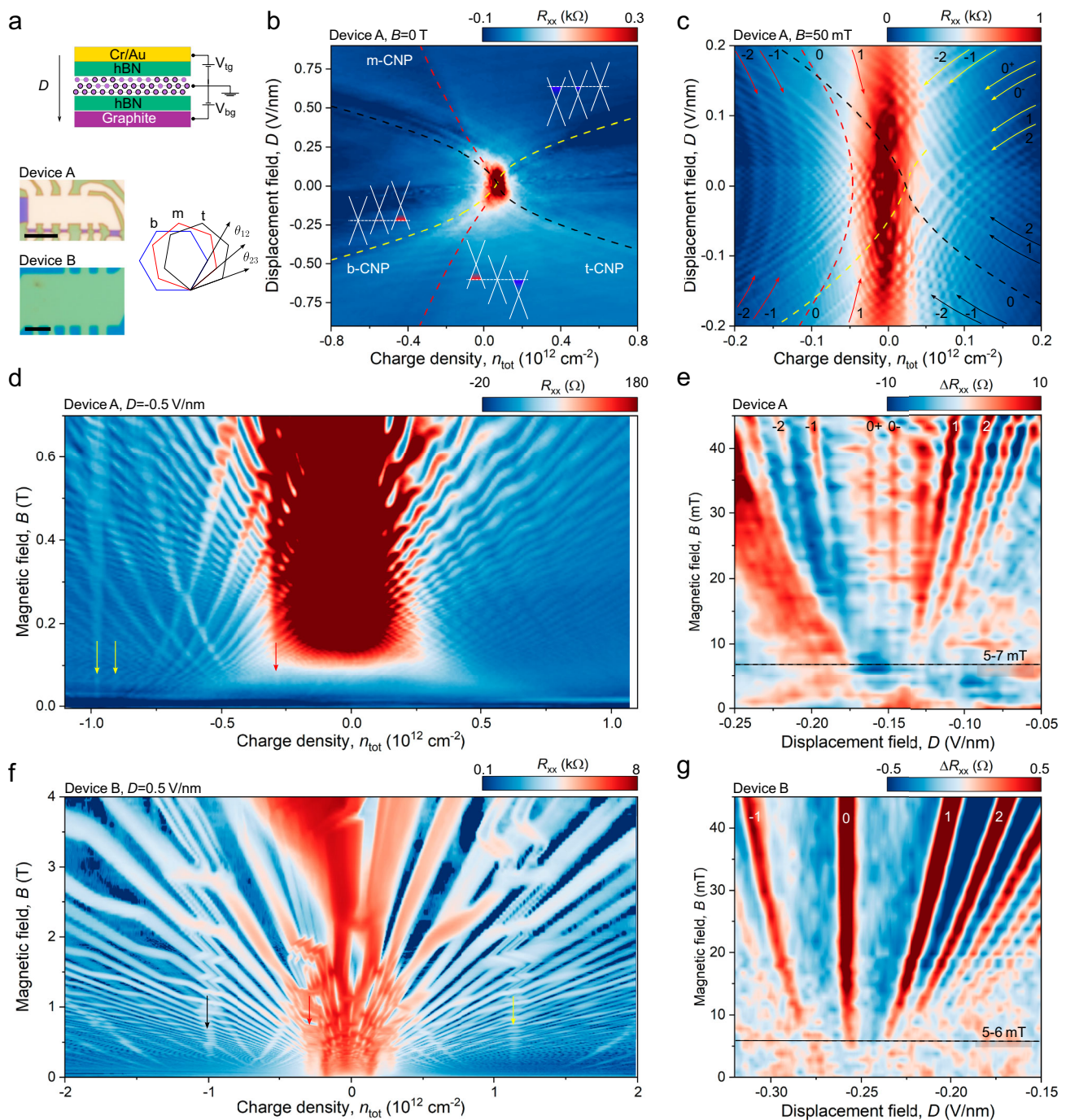


Fig. 3 | High quality of LATTG devices. **a** Schematic structure of LATTG devices, graphene layers (b, m, and t labels indicate bottom, middle, and top layers, respectively) are twisted by large angles θ_{12} (the angle between the bottom and the middle layers) and θ_{23} (the angle between the middle and the top layers). See “Methods” for further information. Optical images show two measured LATTG Hall bar devices A and B, scale bar is 5 μm . **b** Longitudinal resistance at $B = 0$ T as a function of charge density n_{tot} and displacement field D measured in device A. Coloured lines indicate conditions of CNP for top, middle, and bottom layers with black, red, and yellow correspondingly. Inset band structures illustrate the position of CNPs of each layer. **c** Longitudinal resistance at $B = 50$ mT as a function of n_{tot}

and D measured in device A. Coloured dashed lines show the calculated CNP positions for all three layers based on the electrostatic model described in the Supplementary Note 1. We therefore label the nearest Landau levels as $\pm 1, \pm 2$, with the sign reflecting the charge carrier type in each layer. **d–g** Magnetoresistance measurements for devices A and B. **d, f** Measured for fixed $D = -0.5$ V/nm and $D = 0.5$ V/nm correspondingly as a function of n_{tot} , coloured arrows show positions of CNPs. **e, g** Longitudinal resistance measured for fixed n_{tot} as a function of D with removed background (see Supplementary Fig. 10 for more details). Onset of Landau quantisation become resolvable already at $B^* = 5 - 7$ mT in (**e**) and at $B^* = 5 - 6$ mT in (**g**). Measurements were done at 2 K for all panels.

in Fig. 3d and f. Notably, in Fig. 3f, the complete lifting of the zeroth Landau level degeneracy is resolvable at magnetic fields as low as 1 Tesla, while it is not seen in devices without screening at similar field ranges. The high-resolution fan diagrams at small magnetic fields

shown in Fig. 3e and g reveal the onset of Landau quantization already at 5–7 mT (see Supplementary Note 5 and Supplementary Fig. 12) for two different LATTG devices, showcasing the high electronic quality of graphene in such structures.

Discussion

While both LATBG and LATTG devices exhibit similar onsets of quantization in millitesla magnetic field range, LATTG devices demonstrate superior electronic quality. For instance, at $B = 50$ mT LATTG device allows to resolve up to 20–30 LLs per layer, Fig. 3c, whereas LATBG devices show only up to 8 LLs, even at higher $B = 100$ mT, Supplementary Fig. 5. However, in LATTG devices, when the Fermi level is tuned towards the CNP of one of the layers, the other two heavily doped layers act as parallel conduction channels. This obstructs the access to the properties of the charge neutral layer by introducing significant background signals that can interfere with measurements (see Supplementary Fig. 22). Another difference in performance between LATBG and LATTG devices is that the former shows identical gaps at CNPs of both layers (see Fig. 2d), whereas the latter shows a clear gap only in one of the layers (see Fig. 3c and Supplementary Fig. 22). Below, we consider several possibilities for the gap origin.

Multiple theoretical works have predicted a Mott insulator gap at the CNP of graphene^{41,42}. However, experiments with freestanding graphene have shown renormalization of the Fermi velocity instead of a gap, which was attributed to the presence of strong long-range Coulomb interactions²⁹. A recent study suggests that suppressing the tail of Coulomb interactions (e.g., with a metallic screening layer) may result in a semimetal-Mott insulator transition⁴². However, our modelling of such transition predicts gap dependence on temperature and D , which are not observed in the measured devices (see Supplementary Notes 2, 8 and Supplementary Figs. 5 and 6). This points towards a structural origin of the gap, which may appear due to the contact between graphene and hBN (G/hBN) or due to the twist between graphene layers.

Prior studies on the devices where graphene is aligned with encapsulating hBN crystals report varying gap sizes depending on the graphene-hBN alignment^{17,18,43–48}; however, this effect is minimized in our samples, since we intentionally misaligned graphene and hBN during device fabrication. Moreover, in Fig. 2d, the observed gaps in the LATBG device are identical in both layers; this symmetry would likely be broken if misaligned hBN/G interface had a noticeable impact on the band structure. Next, in LATTG devices, the presence of a gap in only one of the outer layers suggests that any gap due to the graphene/hBN interface can indeed be negligible with our intentional misalignment (otherwise, it would be resolved in the other outer layer) pointing to the possible intrinsic origin of this gap within the twisted graphene structure.

To investigate this hypothesis, we calculated the band structure of LATBG at various high commensurate angles (Supplementary Fig. 23). The calculated band structures revealed a small band gap of a few meV opening at the Dirac points of each layer, along with a larger gap at the CNP of the double layer, which was not observed experimentally. It is essential to note that these calculations are influenced by the choice of the unit cell origin, which may change due to the lateral shift between the layers (see Supplementary Note 10).

It should be noted that existing theories on the band structure of LATBG mainly focus on commensurate angles^{49–51} which are challenging to achieve in real devices. Moreover, the precise determination of the electronic structures is highly sensitive to the actual arrangement of atoms, as determined by the lateral shift and twist angle. These challenges make the systematic study of gaps at the Dirac points quite difficult and place it beyond the scope of this work.

Although it is challenging to pinpoint the exact microscopic origin of the gap, the ability to resolve such small features of the band structure highlights the spectroscopic capabilities enabled by encapsulation with graphene layers. Since resolving gaps below 5 meV ($\delta E < 2.5$ meV) at the CNP of Dirac point requires a doping inhomogeneity level below $2 \times 10^9 \text{ cm}^{-2}$, our samples exceed performance of the state-of-the-art devices. More than that, tunable Coulomb screening reduces doping inhomogeneities towards $3 \times 10^8 \text{ cm}^{-2}$, which is an order of magnitude improvement and corresponds to $\delta E \approx 0.5$ meV.

Such high quality allowed to resolve the onset of Landau quantization in our devices at magnetic fields of 5–6 mT, corresponding to a quantum mobility relevant for the observation of quantum phenomena, $\mu_q \approx (1.5\text{--}2) \times 10^6 \text{ cm}^2 \text{ V}^{-1} \text{ s}^{-1}$. Unfortunately, the large-angle twisted multilayer graphene geometry does not allow the direct measurement of the transport mobility of individual graphene layers under applied screening, as a significant portion of the current always propagates through a heavily doped graphene layer. Nevertheless, our toy model (see Supplementary Note 3 and Supplementary Fig. 7) estimates that the transport mobility near CNP in our devices approaches $\mu \approx (12\text{--}20) \times 10^6 \text{ cm}^2 \text{ V}^{-1} \text{ s}^{-1}$, an order of magnitude higher than μ_q . This difference is expected as transport mobility is limited by backscattering, whereas quantum mobility is more sensitive to small-angle scattering. Both quantum and transport mobilities in our devices are an order of magnitude higher than those in devices without screening. We also note that the quantum mobility achieved in our devices is higher than the quantum mobility of the best GaAs 2DEGs, where quantum oscillations onset⁷ around 35–40 mT even at milli-Kelvin temperature, with the quantum mobility⁶ $\mu_q \approx 1 \times 10^6 \text{ cm}^2 \text{ V}^{-1} \text{ s}^{-1}$. At the same time, our estimations give mobility values of the same order as that of the best GaAs samples, highlighting a significant improvement of graphene devices.

Finally, we note that the large twist angle approach also introduces new capabilities, such as tuneable Coulomb interactions via adjustable screening, facilitating further exploration of many-body effects in moiré quantum materials⁵². Our encapsulation method is readily adaptable to other multilayer and twisted heterostructures, thereby broadening its potential applications.

Methods

Sample fabrication

The heterostructures studied in this work were assembled using a combination of the tear-and-stack method together with dry transfer technique^{9,12,53}. Polydimethylsiloxane (PDMS) stamps coated with a thin polycarbonate (PC) membrane were employed to pick up exfoliated crystals from Si/SiO₂ substrates. The pick-up process was conducted at 100 °C in the following sequence: hBN of 30–40 nm thickness (top layer), a large graphene flake (first segment), the second segment of the same graphene flake, rotated to a large twist angle, and another hBN layer (bottom layer, 30–40 nm). Our target angle for the HATBG sample is 20°, for the HATTG devices A and B $\theta_{12} \approx 20^\circ, \theta_{23} \approx -20^\circ$ and $\theta_{12} \approx 30^\circ, \theta_{23} \approx 30^\circ$, respectively; the device C shown in the Supplementary Information had target angles $\theta_{12} \approx 10^\circ, \theta_{23} \approx 10^\circ$. The final vdW stack was released on top of graphite flake at 180°, after which the PDMS stamp was carefully delaminated from the PC membrane. The melted PC film was subsequently dissolved in dichloromethane, followed by rinsing in acetone and isopropyl alcohol.

Next, we used high-resolution atomic force microscopy to locate bubble-free regions suitable for device fabrication. Standard nanofabrication techniques were then used to pattern Hall bars in the identified clean regions. First, the top gates were fabricated using electron-beam lithography (EBL), followed by chromium/gold (Cr/Au) metal deposition. In a subsequent EBL step, deep reactive ion etching with a CHF₃/O₂ gas mixture was employed to define the Hall bar geometry. Finally, one-dimensional electrical contacts to the twisted bilayer graphene (TBG) were formed by depositing Cr/Au onto the exposed graphene edges.

Electronic transport measurements

The electronic transport measurements were performed using standard low-frequency lock-in techniques with excitation currents below 100 nA, minimizing heating and non-linear effects; the measurement temperature was 2 K if not specified. Most of the data presented in the main text were acquired under nonzero displacement field, D . The dual-gated device configuration allowed independent control of D and the total carrier density, n_{tot} . The carrier density was determined as the sum of the densities induced by the top and bottom gates:

$n_{\text{tot}} = \frac{1}{e} (C_{\text{tg}} V_{\text{tg}} + C_{\text{bg}} V_{\text{bg}})$, where V_{tg} and V_{bg} are the voltages applied on a top and bottom gates, and C_{tg} and C_{bg} are the top and bottom gate capacitances per unit area, respectively, found from the Hall effect measurements. The displacement field was calculated as: $D = \frac{1}{2\epsilon_0} (C_{\text{tg}} V_{\text{tg}} - C_{\text{bg}} V_{\text{bg}})$, where ϵ_0 is the vacuum permittivity.

To characterize our devices, we first measured their resistivity at zero displacement and magnetic field and defined inhomogeneity as a half-width at half-maximum (HWHM) as illustrated in Supplementary Fig. 1a. We note that the inhomogeneity of individual layers is half of the HWHM. Next, we calculated mean free path and mobility using a standard expression for the single-layer graphene, but considering that we have two graphene sheets instead of one:

$$\mu = \frac{1}{\rho n_{\text{tot}} e} \quad (1)$$

$$l_{\text{mfp}} = \frac{1}{\rho} \frac{\hbar}{e^2} \sqrt{\frac{\pi}{2n_{\text{tot}}}} \quad (2)$$

Here ρ is the resistivity of the whole double layer, \hbar is reduced Plank constant, and e is an electron charge. The results are shown in Supplementary Fig. 1b, c, which indicate that at zero D the mean free path in our device is approaching device width, and mobility approaching $10^6 \text{ cm}^2 \text{ V}^{-1} \text{ s}^{-1}$ as expected for the high-quality encapsulated devices.

At applied D , we cannot decipher resistivity of the individual layer, however, magnetic focusing measurements allow to claim when the sample is ballistic. In Supplementary Fig. 2, magnetic focusing line approaches the boundaries of the gap as close as the measurement accuracy $\delta n < 2 \times 10^9 \text{ cm}^{-2}$, and corresponds to the mean free path of $l_{\text{mfp}} > L = 2.7 \mu\text{m}$, where L is the distance between centers of the contacts, and the inequality sign is used because the electrons move along cyclotron orbits. Thus, we can set a lower boundary for electron mobility at $D = -0.55 \text{ V/nm}$:

$$\mu = \frac{l_{\text{mfp}} e}{\hbar} \sqrt{\frac{2}{\pi \delta n}} > 7.3 \times 10^6 \text{ cm}^2 / \text{Vs} \quad (3)$$

Data availability

Relevant data supporting the key findings of this study are available within the article and the Supplementary Information file. All raw data generated during the current study are available from the corresponding authors upon request.

References

- Geim, A. K. & Novoselov, K. S. The rise of graphene. *Nat. Mater.* **6**, 183–191 (2007).
- Yankowitz, M., Ma, Q., Jarillo-Herrero, P. & LeRoy, B. J. van der Waals heterostructures combining graphene and hexagonal boron nitride. *Nat. Rev. Phys.* **1**, 112–125 (2019).
- Rhodes, D., Chae, S. H., Ribeiro-Palau, R. & Hone, J. Disorder in van der Waals heterostructures of 2D materials. *Nat. Mater.* **18**, 541–549 (2019).
- Pfeiffer, L., West, K. W., Stormer, H. L. & Baldwin, K. W. Electron mobilities exceeding $107 \text{ cm}^2/\text{V s}$ in modulation-doped GaAs. *Appl. Phys. Lett.* **55**, 1888–1890 (1989).
- Umansky, V. et al. MBE growth of ultra-low disorder 2DEG with mobility exceeding $35 \times 10^6 \text{ cm}^2/\text{Vs}$. *J. Cryst. Growth* **311**, 1658–1661 (2009).
- Sammon, M., Zudov, M. A. & Shklovskii, B. I. Mobility and quantum mobility of modern GaAs/AlGaAs heterostructures. *Phys. Rev. Mater.* **2**, 064604 (2018).
- Chung, Y. J. et al. Ultra-high-quality two-dimensional electron systems. *Nat. Mater.* **20**, 632–637 (2021).
- Chung, Y. J. et al. Understanding limits to mobility in ultrahigh-mobility GaAs two-dimensional electron systems: 100 million cm^2/Vs and beyond. *Phys. Rev. B* **106**, 075134 (2022).
- Wang, L. et al. One-dimensional electrical contact to a two-dimensional material. *Science* **342**, 614–617 (2013).
- Ponomarenko, L. A. et al. Extreme electron-hole drag and negative mobility in the Dirac plasma of graphene. *Nat. Commun.* **15**, 9869 (2024).
- Dean, C. R. et al. Boron nitride substrates for high-quality graphene electronics. *Nat. Nanotechnol.* **5**, 722–726 (2010).
- Purdie, D. G. et al. Cleaning interfaces in layered materials heterostructures. *Nat. Commun.* **9**, 5387 (2018).
- Kumaravadeivel, P. et al. Strong magnetophonon oscillations in extra-large graphene. *Nat. Commun.* **10**, 3334 (2019).
- Kim, M. et al. Control of electron-electron interaction in graphene by proximity screening. *Nat. Commun.* **11**, 2339 (2020).
- Barrier, J. et al. Long-range ballistic transport of Brown-Zak fermions in graphene superlattices. *Nat. Commun.* **11**, 5756 (2020).
- Wang, W. Polymer-free assembly of ultraclean van der Waals heterostructures. *Nat. Rev. Phys.* **4**, 504–504 (2022).
- Zibrov, A. A. et al. Even-denominator fractional quantum Hall states at an isospin transition in monolayer graphene. *Nat. Phys.* **14**, 930–935 (2018).
- Polshyn, H. et al. Quantitative transport measurements of fractional quantum Hall energy gaps in edgeless graphene devices. *Phys. Rev. Lett.* **121**, 226801 (2018).
- Zeng, Y. et al. High-quality magnetotransport in graphene using the edge-free corbino geometry. *Phys. Rev. Lett.* **122**, 137701 (2019).
- Ribeiro-Palau, R. et al. High-quality electrostatically defined hall bars in monolayer graphene. *Nano Lett.* **19**, 2583–2587 (2019).
- Crossno, J. et al. Observation of the Dirac fluid and the breakdown of the Wiedemann-Franz law in graphene. *Science* **351**, 1058–1061 (2016).
- Gallagher, P. et al. Quantum-critical conductivity of the Dirac fluid in graphene. *Science* **364**, 158–162 (2019).
- Ku, M. J. H. et al. Imaging viscous flow of the Dirac fluid in graphene. *Nature* **583**, 537–541 (2020).
- Xin, N. et al. Giant magnetoresistance of Dirac plasma in high-mobility graphene. *Nature* **616**, 270–274 (2023).
- Decker, R. et al. Local electronic properties of graphene on a BN substrate via scanning tunneling microscopy. *Nano Lett.* **11**, 2291–2295 (2011).
- Xue, J. et al. Scanning tunnelling microscopy and spectroscopy of ultra-flat graphene on hexagonal boron nitride. *Nat. Mater.* **10**, 282–285 (2011).
- Adam, S., Hwang, E. H., Galitski, V. M. & Das Sarma, S. A self-consistent theory for graphene transport. *Proc. Natl. Acad. Sci.* **104**, 18392–18397 (2007).
- Martin, J. et al. Observation of electron-hole puddles in graphene using a scanning single-electron transistor. *Nat. Phys.* **4**, 144–148 (2008).
- Elias, D. C. et al. Dirac cones reshaped by interaction effects in suspended graphene. *Nat. Phys.* **7**, 701–704 (2011).
- Mayorov, A. S. et al. How close can one approach the Dirac point in graphene experimentally?. *Nano Lett.* **12**, 4629–4634 (2012).
- Ki, D.-K. & Morpurgo, A. F. High-quality multiterminal suspended graphene devices. *Nano Lett.* **13**, 5165–5170 (2013).
- Ponomarenko, L. A. et al. Tunable metal-insulator transition in double-layer graphene heterostructures. *Nat. Phys.* **7**, 958–961 (2011).
- Agarwal, H. et al. Ultra-broadband photoconductivity in twisted graphene heterostructures with large responsivity. *Nat. Photonics* **17**, 1047–1053 (2023).
- Kim, Y. et al. Breakdown of the interlayer coherence in twisted bilayer graphene. *Phys. Rev. Lett.* **110**, 096602 (2013).
- Sanchez-Yamagishi, J. D. et al. Helical edge states and fractional quantum Hall effect in a graphene electron-hole bilayer. *Nat. Nanotechnol.* **12**, 118–122 (2017).

36. Rickhaus, P. et al. The electronic thickness of graphene. *Sci. Adv.* **6**, eaay8409 (2020).
37. Kim, D. et al. Robust interlayer-coherent quantum Hall states in twisted bilayer graphene. *Nano Lett.* **23**, 163–169 (2023).
38. Inbar, A. et al. The quantum twisting microscope. *Nature* **614**, 682–687 (2023).
39. Boschi, A. et al. Built-in Bernal gap in large-angle-twisted monolayer-bilayer graphene. *Commun. Phys.* **7**, 391 (2024).
40. Hoke, J. C. et al. Uncovering the spin ordering in magic-angle graphene via edge state equilibration. *Nat. Commun.* **15**, 4321 (2024).
41. Drut, J. E. & Lähde, T. A. Is graphene in vacuum an insulator?. *Phys. Rev. Lett.* **102**, 026802 (2009).
42. Tang, H.-K. et al. The role of electron-electron interactions in two-dimensional Dirac fermions. *Science* **361**, 570–574 (2018).
43. Song, J. C. W., Shytov, A. V. & Levitov, L. S. Electron interactions and gap opening in graphene superlattices. *Phys. Rev. Lett.* **111**, 266801 (2013).
44. Jung, J., DaSilva, A. M., MacDonald, A. H. & Adam, S. Origin of band gaps in graphene on hexagonal boron nitride. *Nat. Commun.* **6**, 6308 (2015).
45. Wang, L. et al. Evidence for a fractional fractal quantum Hall effect in graphene superlattices. *Science* **350**, 1231–1234 (2015).
46. Ribeiro-Palau, R. et al. Twistable electronics with dynamically rotatable heterostructures. *Science* **361**, 690–693 (2018).
47. Kim, H. et al. Accurate gap determination in monolayer and bilayer Graphene/ *h* -BN moiré superlattices. *Nano Lett.* **18**, 7732–7741 (2018).
48. Han, T. et al. Accurate measurement of the gap of graphene / *h* -BN moiré superlattice through photocurrent spectroscopy. *Phys. Rev. Lett.* **126**, 146402 (2021).
49. Shallcross, S., Sharma, S., Kandelaki, E. & Pankratov, O. A. Electronic structure of turbostratic graphene. *Phys. Rev. B* **81**, 165105 (2010).
50. Rozhkov, A. V., Sboychakov, A. O., Rakhmanov, A. L. & Nori, F. Single-electron gap in the spectrum of twisted bilayer graphene. *Phys. Rev. B* **95**, 045119 (2017).
51. Talkington, S. & Mele, E. J. Electric-field-tunable band gap in commensurate twisted bilayer graphene. *Phys. Rev. B* **107**, L041408 (2023).
52. Lau, C. N., Bockrath, M. W., Mak, K. F. & Zhang, F. Reproducibility in the fabrication and physics of moiré materials. *Nature* **602**, 41–50 (2022).
53. Cao, Y. et al. Superlattice-induced insulating states and valley-protected orbits in twisted bilayer graphene. *Phys. Rev. Lett.* **117**, 116804 (2016).

Acknowledgements

This work has been supported by the National Research Foundation, Singapore under its NRF Fellowship (NRFF) (NRF-NRFF16-2024-0011), and by A*STAR under its RIE2025 Manufacturing, Trade and Connectivity (MTC) Young Individual Research Grant (M23M7c0126) awarded to A.I.B.; S.S. and V.I.F. acknowledge support from International Science Partnerships Fund (UK), British Council Grant 1185409051, and EPSRC grant EP/V007033/1; M.T. is supported by the Singapore Ministry of Education Research Centre of Excellence award to the Institute for Functional Intelligent Materials (I-FIM, Project No. EDUNC-33-18-279-V12); A.P. and A.K. acknowledge support from the European Commission under the EU Horizon 2020 MSCA-RISE-2019 program (project 873028 HYDROTRONICS) and from the Leverhulme Trust under the grant agreement RPG-2023-253; K.W. and T.T. acknowledge support from the JSPS KAKENHI (Grant Numbers 21H05233 and 23H02052), the CREST (JPMJCR24A5), JST and World Premier International Research Center Initiative (WPI), MEXT, Japan. IMDEA Nanociencia acknowledges support from the ‘Severo Ochoa’ Programme for Centres of Excellence in R&D (CEX2020-001039-S/AEI/10.13039/501100011033); Z.Z. and P.A.P. acknowledge support from NOVOMAT, project PID2022-142162NB-I00 funded by MICIU/AEI/10.13039/

501100011033 and by FEDER, UE as well as financial support through the (MAD2D-CM)-MRR MATERIALES AVANZADOS-IMDEA-NC; Z.Z. acknowledges support from the European Union’s Horizon 2020 research and innovation programme under the Marie-Sklodowska Curie grant agreement No 101034431. K.S.N. acknowledges support from the Royal Society (UK, grant no. RSRP\R\190000). This project is supported by the National Research Foundation, Singapore under its AI Singapore Programme (AISG Award No: AISG3-RP-2022-028). Authors are grateful to Kristina Vaklinova for fabrication advice, to Giovanni Vignale, and Mohammed Mohammed Esmail Al-Ezzi for useful discussions.

Author contributions

A.I.B. designed and supervised the project. I.B. carried out the project and performed the electron transport measurements, with contributions from I.Bg. and J.Z. I.B. fabricated and characterized the devices shown in the main text; I.R. fabricated an additional LATTG device shown in the Supplementary Information. D.B., S.G., and M.S. contributed to sample characterization. K.W. and T.T. provided hBN crystals. A.E.K., A.P., S.S., V.I.F. and M.T. contributed to the theoretical interpretation and performed numerical simulations. Z.Z. and P.A.P. performed band structure calculations for LATBG. I.B. and A.I.B. analysed the data, with contributions from S.S., V.I.F., K.S.N., A.E.K., A.P. and M.T. I.B. and A.I.B. wrote the manuscript with inputs from A.E.P., A.P., S.S., V.I.F. and M.T. All authors discussed the results and contributed to the final version of the manuscript.

Competing interests

The authors declare no competing interests.

Additional information

Supplementary information The online version contains supplementary material available at <https://doi.org/10.1038/s41467-025-62492-5>.

Correspondence and requests for materials should be addressed to I. Babich or A. I. Berdyugin.

Peer review information *Nature Communications* thanks Luca Banszerus and the other, anonymous, reviewers for their contribution to the peer review of this work. A peer review file is available.

Reprints and permissions information is available at <http://www.nature.com/reprints>

Publisher’s note Springer Nature remains neutral with regard to jurisdictional claims in published maps and institutional affiliations.

Open Access This article is licensed under a Creative Commons Attribution-NonCommercial-NoDerivatives 4.0 International License, which permits any non-commercial use, sharing, distribution and reproduction in any medium or format, as long as you give appropriate credit to the original author(s) and the source, provide a link to the Creative Commons licence, and indicate if you modified the licensed material. You do not have permission under this licence to share adapted material derived from this article or parts of it. The images or other third party material in this article are included in the article’s Creative Commons licence, unless indicated otherwise in a credit line to the material. If material is not included in the article’s Creative Commons licence and your intended use is not permitted by statutory regulation or exceeds the permitted use, you will need to obtain permission directly from the copyright holder. To view a copy of this licence, visit <http://creativecommons.org/licenses/by-nc-nd/4.0/>.

© The Author(s) 2025